Photoluminescent Layered Lanthanide Silicate Nanoparticles

Duarte Ananias,[†,‡,§] Stanislav Ferdov,[†,‡,||] Filipe A. Almeida Paz,[†] Rute A. Sá Ferreira,[‡] Artur Ferreira,[⊥] Carlos F. G. C. Geraldes,[§] Luís D. Carlos,[‡] Zhi Lin,*[,†] and João Rocha*[,†]

Departments of Chemistry and Physics and ESTGA, CICECO, University of Aveiro, 3810-193 Aveiro, Portugal, and Department of Biochemistry, University of Coimbra, 3001-401 Coimbra, Portugal

Received September 4, 2007. Revised Manuscript Received October 31, 2007

The first examples of nanoparticles of pure layered $Ln_2(SiO_4H)(OH)_2(H_2O)Cl$ (where Ln = Eu, Gd, and Tb) and mixed microcrystalline layered lanthanide silicates containing different Eu/Gd and Tb/Gd ratios have been reported. The crystal structure of these silicates has been solved from synchrotron powder X-ray diffraction data. These materials display interesting and tuneable photoluminescence (PL) properties, such as energy transfer between different Ln^{3+} centers, illustrated here with the pairs Eu^{3+}/Gd^{3+} and Tb^{3+}/Gd^{3+}. The PL properties of the mixed Eu^{3+}/Gd^{3+} sample change upon F^- for Cl^- ion exchange, and this raises the possibility that this material may be exploited for sensing these ions.

Introduction

Although largely overlooked, stoichiometric layered lanthanide (Ln) silicates are host–guest systems suitable for engineering multifunctional materials with tuneable properties.[1] These solids, which contain Ln^{3+} cations in the layers and interlayer spaces, combine the properties of layered silicates (such as intercalation chemistry or ion exchange) and photoluminescence (PL) and may, thus, find applications in new types of sensors. Much of the work concerning stoichiometric Ln-containing layered materials exhibiting PL has been concentrated on coordination polymers[2,3] and three-dimensional phosphonates, consisting of inorganic layers connected by organic groups, reminiscent of pillared structures.[4] In order to embed layered Ln silicates in sensors and other devices, it is of interest to prepare nanoparticles of these materials, which may be used, for example, in ink-jet printing or incorporated in polymer matrixes. However, to the best of our knowledge, such nanoparticles are not available. We have previously reported on the first example of a microcrystalline layered Ln silicate system, $K_3[LnSi_3O_8(OH)_2]$.[1] Here, we present the synthesis of nanoparticles (ca. 30 nm) of pure layered $Ln_2(SiO_4H)(OH)_2(H_2O)Cl$ (where Ln = Eu, Gd, and Tb) and of mixed microcrystalline layered Ln silicates containing different Eu^{3+}/Gd^{3+} and Tb^{3+}/Gd^{3+} ratios. These materials display interesting PL properties, for example, energy transfer between different Ln^{3+} centers, illustrated here with the pairs Eu^{3+}/Gd^{3+} and Tb^{3+}/Gd^{3+}. The crystal structure of these materials has been solved from synchrotron powder X-ray diffraction (XRD) data.

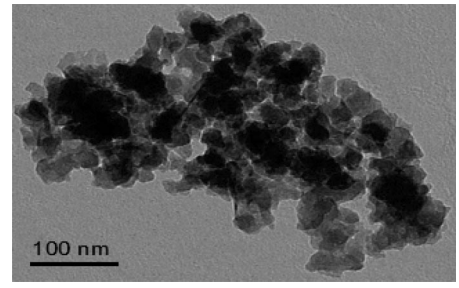

Figure 1. TEM image of $Eu_2(SiO_4H)(OH)_2(H_2O)Cl$ showing 20–40 nm nanoparticles.

Experimental Section

Sample Preparation. The syntheses of Ln silicates were carried out in Teflon-lined autoclaves, under static hydrothermal conditions, in ovens preheated at 230 °C. All Ln salts were of 99.9% purity. In all syntheses, autoclaves were removed and quenched in cold water after an appropriate time. The obtained powders were filtered, washed at room temperature with distilled water, and dried at 60 °C.

$Ln_2(SiO_4H)(OH)_2(H_2O)Cl$ (where Ln = Eu, Gd, and Tb) nanocrystals (Figure 1) were prepared from gels with the following molar composition: 1.49:1:1.88:400 $K_2O/Ln_2O_3/SiO_2/H_2O$. In a typical synthesis ($Eu_2SiO_4H(OH)_2Cl\cdot H_2O$), an alkaline solution, made by mixing 0.17 g of silica gel (91.8 wt % SiO_2; Aldrich), 0.27 g of KOH (85 wt %; Pronalab), and 6 g of H_2O, was added to a solution of 1 g of $EuCl_3\cdot 6H_2O$ (Aldrich) dissolved in 4 g of H_2O, forming an acidic gel (pH ~ 6). The as-prepared gel was stirred thoroughly for ca. 120 min, then transferred into autoclaves, and heated for 10 days. The samples with Ln = Tb^{3+}, Tb^{3+}/Gd^{3+}, and Eu^{3+}/Gd^{3+} were prepared by adding a desired combination of Ln ions into the precursor.

* Corresponding author. E-mail: zlin@ua.pt (Z.L.), rocha@ua.pt (J.R.). Tel: (+351) 234 401 519 (Z.L.), (+351) 234 370 730 (J.R.). Fax: (+351) 234 370 084 (Z.L.), (+351) 234 370 084 (J.R.).
† Department of Chemistry, CICECO, University of Aveiro.
‡ Department of Physics, CICECO, University of Aveiro.
§ University of Coimbra.
|| On leave from the Central Laboratory of Mineralogy and Crystallography, Bulgarian Academy of Sciences.
⊥ ESTGA, CICECO, University of Aveiro.

(1) Ananias, D.; Kostova, M.; Paz, F. A. A.; Ferreira, A.; Carlos, L. D.; Klinowski, J.; Rocha, J. *J. Am. Chem. Soc.* **2004**, *126*, 10410–10417.
(2) Pan, L.; Huang, X. X.; Li, J.; Wu, Y.; Zheng, N. *Angew. Chem., Int. Ed.* **2000**, *39*, 527–530.
(3) Huang, Z.; Strobele, M.; Zhang, K. L.; Meyer, H. J.; You, X. Z.; Yu, Z. *Inorg. Chem. Commun.* **2002**, *5*, 230–234.
(4) (a) Serpaggi, F.; Férey, G. *Inorg. Chem.* **1999**, *38*, 4741–4744. (b) Ngo, H. L.; Lin, W.-B. *J. Am. Chem. Soc.* **2002**, *124*, 14298–14299. (c) Tang, S.-F.; Song, J.-L.; Mao, J.-G. *Eur. J. Inorg. Chem.* **2006**, 2011–2019.

10.1021/cm702524n CCC: $40.75
Published on Web 12/11/2007

$Eu_2(SiO_4H)(OH)_2(H_2O)Cl$ microcrystals were prepared as follows. An alkaline solution was made by mixing 0.99 g of a sodium silicate solution (27 wt % SiO_2 and 8 wt % Na_2O; Merck), 17.50 g of H_2O, 0.15 g of NaOH (Panreak), and 0.50 g of NaCl (Panreak). A total of 1.53 g of $EuCl_3 \cdot 6H_2O$ (Aldrich) in 10.0 g of H_2O was added to this solution, and the resulting mixture was stirred thoroughly. The final pH was adjusted to 5.8. The gel was reacted in autoclaves (volume: 42 cm^3) for 7 days. $(Gd_{0.875}Eu_{0.125})_2SiO_4H(OH)_2Cl \cdot H_2O$ was prepared using a similar initial gel, introducing the desired Gd^{3+} and Eu^{3+} contents.

General Instrumentation. The chemical analysis (energy-dispersive spectometry, EDS) yields a Si:Ln (Ln = Eu and Gd or Tb and Gd) molar ratio of ca. 0.47:1.0 in accordance with XRD data, within experimental error. Thermogravimetric analysis (TGA) reveals a total weight loss of ca. 8.4% between 100 and 650 °C for the $Eu_2(SiO_4H)(OH)_2(H_2O)Cl$ material, corresponding to 2.5 water molecules per formula unit.

Transmission electron microscopy (TEM) was carried out using a Philips CM20 twin microscope operating at 200 kV. Scanning electron microscopy images were recorded on a Hitachi S-4100 microscope. EDS was carried out using an EDS Römteck System with a polymeric window attached to the scanning electron microscope. TGA curves were measured on a Labsys TG-DTA 1600 °C rod, from TA instruments. Samples were heated in air with a 10 °C/min rate.

High-resolution powder synchrotron XRD data were collected at ambient temperature (273 K) on the powder diffractometer instrument assembled in the ID31 beam line (insertion device source) at the European Synchrotron Radiation Facility (ESRF), Grenoble, France.[5,6] The beam line receives X-rays from the synchrotron source, operating with an average energy of 6 GeV and a current beam of typically 200 mA, from an undulator device. The high signal-to-noise ratio of the data is due to the high brilliance of the synchrotron beam in combination with the use of a Si(111) crystal multianalyzer. The monochromatic wavelength was fixed at 0.80172(3) Å.

A sample of $Eu_2(SiO_4H)(OH)_2(H_2O)Cl$ nanocrystals was placed inside a Hilgenberg borosilicate glass capillary (0.4 mm of diameter), which was rotated at 3 kHz during data collection to improve powder averaging over the individual crystallites, thus avoiding textural effects (e.g., preferential orientation). Data were collected in a continuous-scanning mode (ca. $2\theta = 10°$/min so as to eliminate the dead time of a conventional step scan) over the angular range $2\theta = 4$–$40°$, with accumulation times increasing with the scattering angle. The counts of eight detectors (covering roughly $2\theta = 8°$) were rebinned and normalized to give the equivalent step scans suitable for further structural analyses.

The collected high-resolution powder XRD pattern for $Eu_2(SiO_4H)(OH)_2(H_2O)Cl$ was indexed by means of the routines provided with the software program *DICVOL04*[7] and by employing the first 25 well-resolved reflections (located using the derivative-based peak search algorithm provided with Fullprof.2k) and a fixed absolute error on each line of $2\theta = 0.01°$. The unit cell metrics summarized in Table 1 were obtained with high figures of merit: $M(25)$[8] = 233.2 and $F(25)$[9] = 976.6; zero shift of 0.0027°. Analysis of the systematic absences from a Le Bail whole-powder-diffraction-pattern extraction in *P*2 using *FullProf.2k*,[10,11] in conjunction with the ADDSYM[12,13] validation routines provided with *PLATON*,[14,15] led to the unambiguous identification of the *Pbcm* space group.

Structure solution was successfully carried out using the direct methods of SIRPOW, included in the software package *eXpo2004*

Table 1. X-ray Data Collection, Crystal Data, and Structure Refinement Details for $Eu_2(SiO_4H)(OH)_2(H_2O)Cl$

Data Collection	
diffractometer	ID31 beam line, ESRF, Grenoble, France
wavelength (Å)	0.801 72(3)
temperature (K)	293
geometry	Debye–Scherrer
2θ range (deg)	4.000−40.000
step size (deg)	0.003

Unit Cell	
formula	$H_5ClEu_2O_7Si$
fw	484.49
cryst syst	orthorhombic
space group	*Pbcm* (No. 57)
a (Å)	8.28651(4)
b (Å)	12.66540(6)
c (Å)	7.09450(3)
V (Å^3)	744.6(1)
Z	4
D_c (g/cm^3)	4.322

Profile Parameters	
profile function	pseudo-Voigt PV = ηL + $(1-\eta)G$: with $\eta = 0.999$
Caglioti law parameters	$U = 0.0057(2)$, $V = -0.000\,93(6)$, $W = 0.000\,17(1)$
asymmetry parameters (up to $2\theta = 40°$)	0.0104(9) and 0.0003(2)
zero point	−0.0040(1)

Refinement Details	
no. of independent reflections	277
no. of global refined parameters	1
no. of profile refined parameters	9
no. of intensity-dependent refined parameters	24

Reliability Factors for Points with Bragg Contribution (Conventional Background Excluded)	
R_p	5.39
R_{wp}	6.85
R_{exp}	5.64
χ^2	1.48

Structure Reliability Factors	
R_{Bragg}	6.82
R_F	6.83

(5) Fitch, A. N. *J. Res. Natl. Inst. Stand. Technol.* **2004**, *109*, 133–142.
(6) Fitch, A. N. The high resolution powder diffraction beam line at ESRF. In *European Powder Diffraction: Epdic Iv, Pts 1 and 2*; Transtec Publications Ltd.: Zurich-Uetikon, 1996; Vol. 228, pp 219−221.
(7) Boultif, A.; Louer, D. *J. App. Crystallogr.* **2004**, *37*, 724–731.
(8) Boultif, A.; Louer, D. *J. App. Crystallogr.* **1991**, *24*, 987–993.
(9) Louer, D. Automatic Indexing: Procedures and Applications. *Accuracy in Powder Diffraction II*; NIST: Gaithersburg, MD, 1992; pp 92–104.
(10) Rodriguez-Carvajal, J. FULLPROF−A Program for Rietveld Refinement and Pattern Matching Analysis. *Abstract of the Satellite Meeting on Powder Diffraction of the XV Congress of the IUCR*, Toulouse, France, 1990; p 127.
(11) Roisnel, T.; Rodriguez-Carvajal, J. WinPLOTR [June 2005]−A Windows Tool for Powder Diffraction Pattern Analysis. In *Materials Science Forum, Proceedings of the Seventh European Powder Diffraction Conference (EPDIC 7)*; Delhez, R., Mittenmeijer, E. J., Eds.; 2000; pp 118−123.
(12) Le Page, Y. *J. Appl. Crystallogr.* **1988**, *21*, 983–984.
(13) Le Page, Y. *J. Appl. Crystallogr.* **1987**, *20*, 264–269.
(14) Spek, A. L. *J. Appl. Crystallogr.* **2003**, *36*, 7–13.
(15) Spek, A. L. *PLATON, A Multipurpose Crystallographic Tool*; Utrecht University: Utrecht, The Netherlands, 2003.

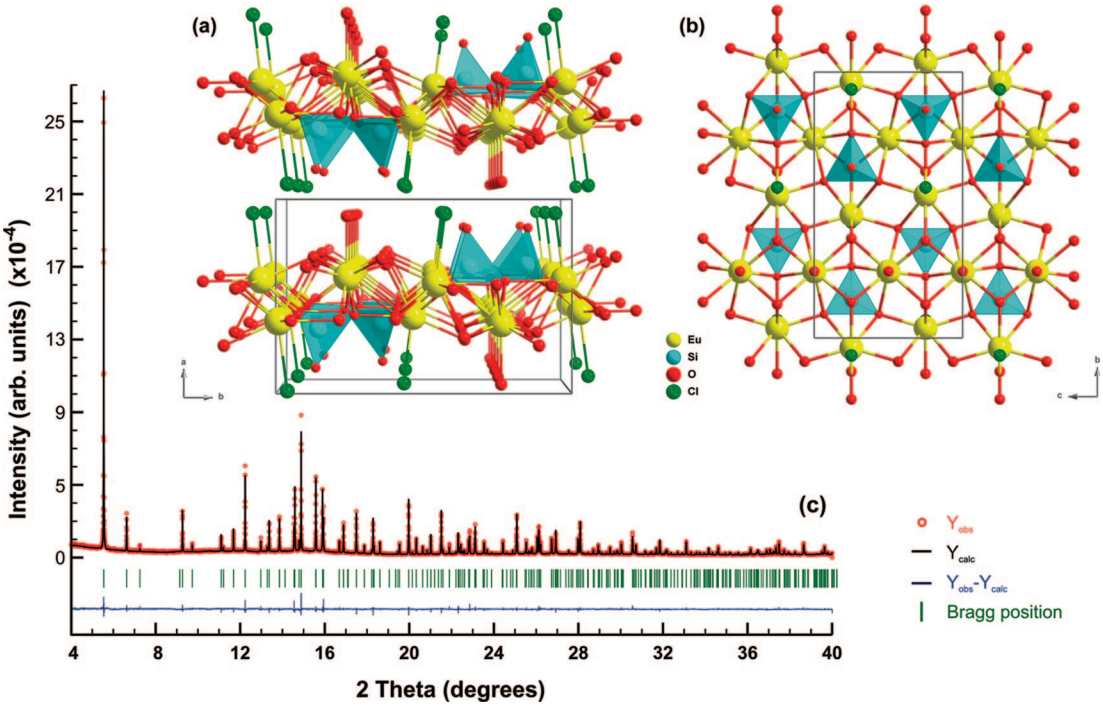

Figure 2. Perspective views (a) along the [001] direction of the crystal packing of $Eu_2(SiO_4H)(OH)_2(H_2O)Cl$ and (b) toward the *bc* plane showing a top view of the $[Eu_2(SiO_4H)(OH)_2(H_2O)Cl]_\infty$ layer. (c) Final Rietveld plot (from powder synchrotron powder X-ray data of the nanocrystals shown in Figure 1).

(version 2.1).[16] After subtraction of the background using individual polynomial functions in selected angular intervals, the intensity of each individual reflection was extracted by employing Pearson profile functions.

Rietveld structural refinement was performed with *FullProf.2k*,[10,11] applying fixed background points throughout the entire angular range, and determined by the linear interpolation between consecutive (and manually selected) breakpoints in the powder pattern. Typical pseudo-Voigt profile functions, along with two asymmetry correction parameters, were selected to generate the line shapes of the simulated diffraction peaks. The angular dependence of the full width at half-maximum of peaks was also taken into account by employing a Caglioti function correction.[17] Structural refinement using the atomic coordinates obtained with *eXpo2004* was done in consecutive stages to avoid refinement instability and divergence. Zero shift, scale factor, all peak-shape parameters, and unit cell parameters were consecutively added as fully refineable variables upon previous full convergence of the remaining parameters to their optimal values. Fractional atomic coordinates were ultimately allowed to refine in conjunction with weighted soft distance constraints for the Eu−O, Eu−Cl, and Si−O bond lengths, thus assuring chemically feasible environments for Eu and Si. Isotropic displacement parameters, common to each element in the structure, were also added to the structural model as fully refineable parameters. After full convergence, the aforementioned soft restraints were removed from the structural model, which was then subjected to further refinement cycles, ultimately converging to the profile and reliability factors summarized in Table 1.

It is noteworthy to mention that bond valence sum (BVS) calculations, based upon the phenomenological model by Brese and O'Keefe[18] and Brown and Altermatt,[19] fully support the structural model. Indeed, the BVSs for O(1), O(4), and O(5) clearly indicate that the former is a terminal Si−OH group ($\Sigma = 1.00$) while the two latter atoms correspond instead to μ_3-bridging hydroxyl groups ($\Sigma = 1.17$ and 1.20, respectively). Even though these H atoms (along with those associated with the coordinated water molecule) were not added to the structural model, they have been included in the empirical formula of the material (see Table 1). Interestingly, the BVSs for the Eu and Si sites are slightly lower than the expected values, which suggests that these centers are slightly underbonded, with the corresponding Eu−O and Si−O bonds being under tensile stress, in good agreement with the presence of a dense layered material where all O atoms bridge three neighboring Eu centers (see the structural description in the main text).

Table 2. Bond Lengths (Å) for the Two Distinct Eu^{3+} Coordination Environments Present in $Eu_2(SiO_4H)(OH)_2(H_2O)Cl$

Eu(1)−O(2)	2.606(10)	Eu(2)−O(2)	2.480(10)
Eu(1)−O(3)	2.437(10)	Eu(2)−O(2)^{i}	2.334(9)
Eu(1)−O(4)	2.412(9)	Eu(2)−O(3)^{ii}	2.451(13)
Eu(1)−O(5)	2.425(9)	Eu(2)−O(4)^{iii}	2.443(13)
Eu(1)−O(1W)	2.492(14)	Eu(2)−O(5)	2.392(13)
		Eu(2)−Cl(1)	2.811(8)

[a] Symmetry transformations used to generate equivalent atoms: (i) $1-x, 1-y, -z$; (ii) $1-x, {}^1/_2+y, {}^1/_2-z$; (iii) $1-x, 1-y, {}^1/_2+z$.

The final Rietveld plot is presented in Figure 2 (magnifications are provided in Figure S1 of the Supporting Information). Refined fractional atomic coordinates (along with site occupancy and isotropic displacement parameters) are listed in Table S1 of the Supporting Information. Bond lengths and selected bond angles for the Eu^{3+} coordination environments are provided in Tables 2 and 3. Table S2 of the Supporting Information lists the possible hydrogen-bonding interactions that link adjacent two-dimensional $[Eu_2(SiO_4H)(OH)_2(H_2O)Cl]_\infty$ layers.

Crystallographic information (excluding structure factors) for $Eu_2(SiO_4H)(OH)_2(H_2O)Cl$ may be obtained free of charge from

(16) Altomare, A.; Burla, M. C.; Camalli, M.; Carrozzini, B.; Cascarano, G. L.; Giacovazzo, C.; Guagliardi, A.; Moliterni, A. G. G.; Polidori, G.; Rizzi, R. *J. Appl. Crystallogr.* **1999**, *32*, 339–340.
(17) Caglioti, G.; Paoletti, A.; Ricci, F. P. *Nucl. Instrum.* **1958**, *3*, 223–228.
(18) Brese, N. E.; O'Keeffe, M. *Acta Crystallogr., Sect. B* **1991**, *47*, 192–197.
(19) Brown, I. D.; Altermatt, D. *Acta Crystallogr., Sect. B* **1985**, *41*, 244–247.

Table 3. Selected Bond Angles (deg) for the Two Distinct Eu^{3+} Coordination Environments Present in $Eu_2(SiO_4H)(OH)_2(H_2O)Cl$

$O(2)^{i}-Eu(1)-O(2)$	106.7(6)	$O(2)-Eu(2)-O(2)^{ii}$	63.8(4)
$O(3)-Eu(1)-O(2)$	62.8(5)	$O(2)^{iii}-Eu(2)-O(2)^{iv}$	146.7(7)
$O(3)-Eu(1)-O(2)^{i}$	69.3(5)	$O(2)^{iii}-Eu(2)-O(2)^{ii}$	130.6(7)
$O(3)^{i}-Eu(1)-O(3)$	94.5(3)	$O(2)^{iii}-Eu(2)-O(2)$	68.8(5)
$O(3)-Eu(1)-O(1W)$	132.7(9)	$O(2)^{iii}-Eu(2)-O(3)^{v}$	73.7(5)
$O(4)-Eu(1)-O(2)$	74.7(5)	$O(2)^{iii}-Eu(2)-O(4)^{iii}$	79.3(5)
$O(4)-Eu(1)-O(2)^{i}$	119.5(7)	$O(2)^{iii}-Eu(2)-O(5)$	106.4(7)
$O(4)-Eu(1)-O(3)$	136.8(6)	$O(3)^{iv}-Eu(2)-O(2)$	129.3(8)
$O(4)-Eu(1)-O(3)^{i}$	62.0(6)	$O(4)^{iii}-Eu(2)-O(2)$	78.9(6)
$O(4)-Eu(1)-O(4)^{i}$	157.9(7)	$O(4)^{iii}-Eu(2)-O(3)^{v}$	61.4(6)
$O(4)-Eu(1)-O(5)$	94.9(3)	$O(5)-Eu(2)-O(2)$	68.5(5)
$O(4)-Eu(1)-O(5)^{i}$	77.9(6)	$O(5)-Eu(2)-O(3)^{v}$	157.3(9)
$O(4)-Eu(1)-O(1W)$	79.0(6)	$O(5)-Eu(2)-O(3)^{v}$	141.3(9)
$O(5)-Eu(1)-O(2)$	66.0(5)	$Cl(1)-Eu(2)-O(2)$	129.0(5)
$O(5)-Eu(1)-O(2)^{i}$	142.4(7)	$Cl(1)-Eu(2)-O(2)^{iii}$	91.7(4)
$O(5)-Eu(1)-O(3)$	75.3(6)	$Cl(1)-Eu(2)-O(3)^{v}$	83.9(6)
$O(5)-Eu(1)-O(3)^{i}$	133.8(6)	$Cl(1)-Eu(2)-O(4)^{iii}$	145.3(7)
$O(5)^{i}-Eu(1)-O(5)$	142.3(6)	$Cl(1)-Eu(2)-O(5)$	73.4(5)
$O(5)-Eu(1)-O(1W)$	71.2(5)		
$O(1W)-Eu(1)-O(2)$	126.6(7)		

[a] Symmetry transformations used to generate equivalent atoms: (i) x, $^1/_2 - y$, $-z$; (ii) x, y, $^1/_2 - z$; (iii) $1 - x$, $1 - y$, $^1/_2 + z$; (iv) $1 - x$, $1 - y$, $-z$; (v) $1 - x$, $^1/_2 + y$, $^1/_2 - z$.

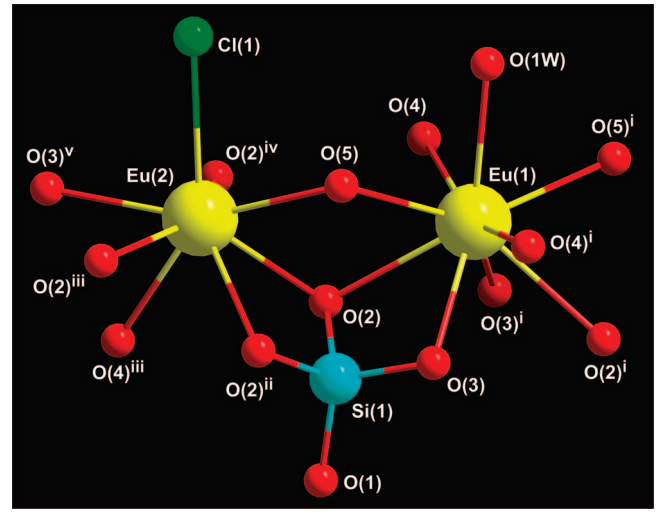

Figure 3. View of the coordination environments of the two crystallographically unique Eu^{3+} Ln centers. For bond lengths (in Å) and selected angles, see Tables 2 and 3, respectively. Symmetry transformations used to generate equivalent atomic positions: (i) x, $^1/_2 - y$, $-z$; (ii) x, y, $^1/_2 - z$; (iii) $1 - x$, $1 - y$, $^1/_2 + z$; (iv) $1 - x$, $1 - y$, $-z$; (v) $1 - x$, $^1/_2 + y$, $^1/_2 - z$.

Fachinformationszentrum Karlsruhe, 76344 Eggenstein-Leopoldshafen, Germany (e-mail: crysdata@fiz-karlsruhe.de), on quoting the depository number CSD-416654.

Phase identification using a Le Bail whole-powder-diffraction-pattern profile fitting for $(Eu_{0.125}Gd_{0.875})_2(SiO_4H)(OH)_2(H_2O)Cl$ was performed with conventional XRD data, collected on an X'Pert MPD Philips diffractometer (Cu Kα radiation, $\lambda = 1.540\,60$ Å) equipped with curved graphite-monochromated radiation and a flat-plate sample holder, in a Bragg–Brentano parafocusing optics configuration. Further details are provided in the Supporting Information.

PL measurements were recorded on a Fluorolog-3 model FL3-2T spectrometer with double excitation (Triax 320), fitted with a 1200 grooves/mm grating blazed at 330 nm, and a single-emission spectrometer (Triax 320), fitted with a 1200 grooves/mm grating blazed at 500 nm, coupled to a R928 photomultiplier. Excitation spectra were corrected from 240 to 600 nm for the spectral distribution of the lamp intensity using a photodiode reference detector. On the basis of the excitation source characteristics, we estimate that the intensity of the spectrum recorded in the 200–240 nm region should be multiplied by a factor of 2. Emission spectra were also corrected for the spectral response of the monochromators and the detector using typical correction spectra provided by the manufacturer. Time-resolved measurements were carried out using a 1934D3 phosphorimeter coupled to the Fluorolog-3, and a Xe−Hg flash lamp (6 μs/pulse half-width and 20–30 μs tail) was used as the excitation source. The measurements at 10 K were performed using a He closed-cycle cryostat.

Absolute emission quantum yields were measured at room temperature using a Quantum Yield Measurement System C9920-02 from Hamamatsu with a 150 W Xe lamp coupled to a monochromator for wavelength discrimination, an integrating sphere as a sample chamber, and a multichannel analyzer for signal detection. The experimental error is within 5%. Three measurements were carried out for each sample, so that the presented quantum yield value corresponds to the arithmetic mean value.

Results and Discussion

TEM images of the $Eu_2(SiO_4H)(OH)_2(H_2O)Cl$ nanocrystals are shown in Figure 1. The particles are agglomerates because of the lack of any protecting layer at their surface. The particle size ranges from 20 to 40 nm. It should be pointed out that the nanocrystals are beam-sensitive because of their structure and composition, and high-resolution images could not be recorded.

$Eu_2(SiO_4H)(OH)_2(H_2O)Cl$ is constructed by parallel packing, along the [100] direction, of two-dimensional undulated layers, placed in the *bc* plane of the orthorhombic unit cell (Figure 2) and having the same empirical formula as the compound. The crystal structure contains two crystallographically unique Eu^{3+} centers, Eu(1) and Eu(2), respectively $\{EuO_9\}$ and $\{EuO_7Cl\}$, which are significantly distorted because of the structural features of the layer. In strict terms, Eu(1) and Eu(2) are not located at crystallographic inversion centers. However, the first coordination sphere of Eu(1) is approximately centrosymmetric. The constraints imposed by the geometry of the $\{SiO_4H\}$ tetrahedron, which bridges six neighboring Ln centers (each Si−O bond acts as a μ_3 bridge; Figure 2b), lead to relatively long Eu−O(2) distances (2.60 and 2.48 Å for Eu(1) and Eu(2), respectively). Thus, the Ln^{3+} coordination geometries are best described as a distorted tricapped trigonal prism (with the capping positions being occupied by the water molecule and the long Eu−O(2) interactions) for Eu(1) and, for Eu(2), as a distorted dodecahedron (Figure 3; for bond lengths and angles, see Tables 2 and 3). Both Eu^{3+} centers markedly have an exo-coordinated ligand pointing toward the interlayer space: while Eu(1) is coordinated to a water molecule [Eu(1)−O(1W) of 2.49 Å], Eu(2) interacts instead with a Cl^- anion with a Eu(2)−Cl(1) distance of 2.81 Å, typical for ionic interactions.

Interactions between neighboring layers are assured by a network of hydrogen bonds involving the terminal Si−OH group and the coordinated water molecule and Cl^- anion (Figure 4 and Table 3). Several lanthanide silicates with the Cl^- ions interacting with four or more Ln^{3+} centers are known.[20–23] The present family of materials is indeed unique

(20) Sieke, C.; Hartenbach, I.; Schleid, T. *Z. Anorg. Allg. Chem.* **2000**, *626*, 2235–2239.

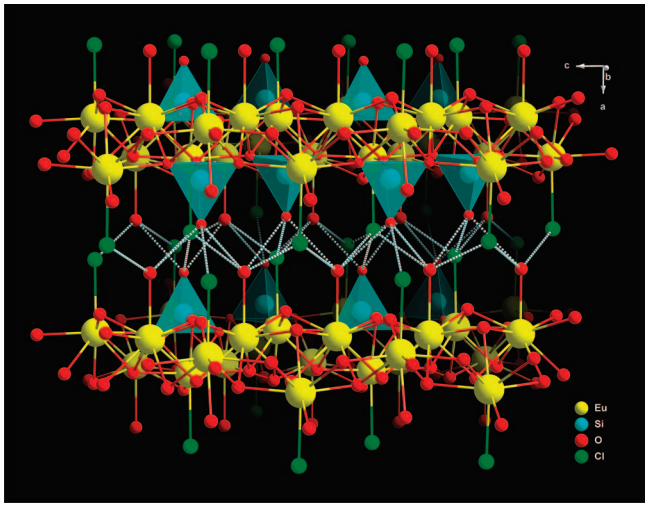

Figure 4. Schematic representation of the hydrogen bonds (white-filled dashed lines) linking adjacent two-dimensional $[Eu_2(SiO_4H)(OH)_2(H_2O)Cl]_\infty$ layers. For geometric details on hydrogen-bonding interactions, see Table S2 of the Supporting Information.

because it consists of the first stoichiometric layered silicates containing chloride in the coordination sphere of a single Ln^{3+} ion.

The PL spectra of nanosized and micron-sized particles are virtually identical and, thus, here we shall not make any distinction between the two types of samples. Parts A and B of Figure 5 compare the excitation spectra of the Eu^{3+}-based silicates as a function of the Eu^{3+} content recorded at room temperature and 10 K, respectively. Samples $(Eu_xGd_{1-x})_2(SiO_4H)(OH)_2(H_2O)Cl$ ($x = 0.125$ and 1) are isostructural (Figures S1 and S2 of the Supporting Information). The spectra of these materials display a series of sharp lines, assigned to the $^7F_{0-1} \rightarrow {}^5D_{4-0}$, $^5L_6$, $^5G_{2-6}$, $^5H_{3-7}$, and $^5F_{1-5}$ Eu^{3+} intra-$4f^6$ transitions, superimposed on two large broad bands at ca. 250 and 315 nm. These broad bands are assigned to, respectively, the spin-allowed interconfigurational $4f^6 \rightarrow 4f^55d^1$ band of Eu^{3+} [1] and the $O^{2-} \rightarrow Eu^{3+}$ ligand-to-metal charge-transfer (LMCT) bands.[24–26] The band at ca. 315 nm is not observed at room temperature, suggesting that this Eu^{3+} excitation path is thermally deactivated and thus supporting the LMCT attribution.[27] The excitation spectra of the Eu^{3+}/Gd^{3+}-based silicates also display lines at 272–279 and 302–312 nm assigned to respectively the $^8S_{7/2} \rightarrow {}^6I_{7/2-17/2}$ and $^6P_{3/2-7/2}$ intra-$4f^7$ transitions of Gd^{3+}, revealing energy transfer from the Gd^{3+} ions to the Eu^{3+} ions. Increasing the Eu^{3+} concentration results in a decrease in the relative intensity of the intra-$4f^7$ Gd^{3+} lines because of the lower number of Gd^{3+} ions transferring energy to the Eu^{3+} ions (Figure 5). Figure 6 shows the room-temperature excitation spectra of the $(Tb_xGd_{1-x})_2(SiO_4H)(OH)_2(H_2O)Cl$ ($x = 0.100$, 0.500, and 1) silicates monitored

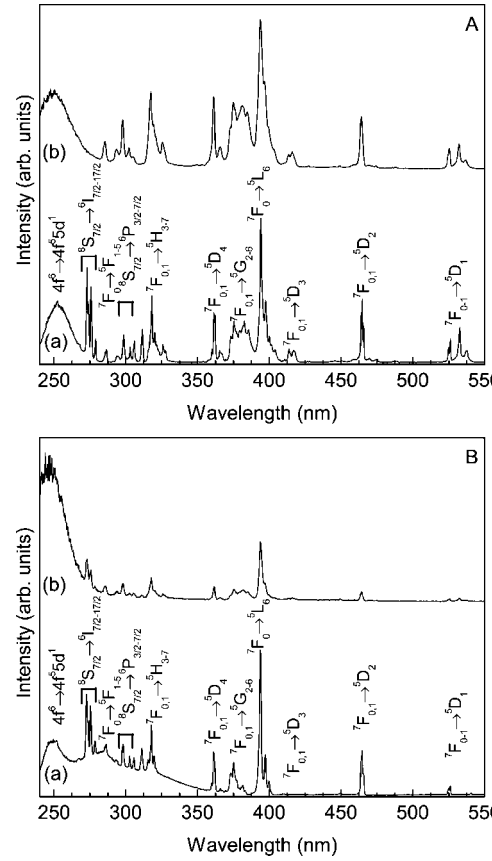

Figure 5. Excitation spectra monitored at 613.2 nm of the $(Eu_{0.125}Gd_{0.875})_2(SiO_4H)(OH)_2(H_2O)Cl$ (a) and $Eu_2(SiO_4H)(OH)_2(H_2O)Cl$ (b) recorded at (A) room temperature and (B) 10 K.

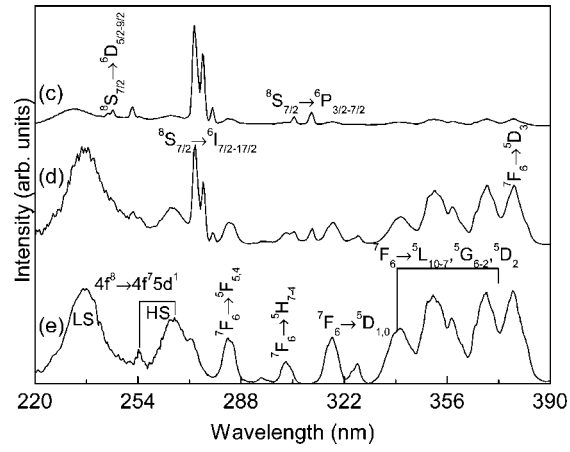

Figure 6. Excitation spectra monitored at 542 nm of $(Tb_{0.1}Gd_{0.9})_2(SiO_4H)(OH)_2(H_2O)Cl$ (c), $(Tb_{0.5}Gd_{0.5})_2(SiO_4H)(OH)_2(H_2O)Cl$ (d), and $Tb_2(SiO_4H)(OH)_2(H_2O)Cl$ (e) recorded at room temperature.

within the intra-$4f^8$ $^5D_4 \rightarrow {}^7F_5$ transition. The spectra display a series of sharp Tb^{3+} lines and two broad bands at ca. 236 and 250–290 nm, assigned to respectively the spin-allowed (low-spin, LS) and spin-forbidden (high-spin, HS) interconfigurational Tb^{3+} fd transitions.[28] As observed for the silicates containing Eu^{3+} (Figure 5), the decrease in the relative amount of Gd^{3+} ions reduces the contribution of the intra-$4f^7$ lines to the excitation spectra monitored within the Tb^{3+} lines.

(21) Sieke, C.; Schleid, T. *Z. Anorg. Allg. Chem.* **1999**, *625*, 377–378.
(22) Sieke, C.; Schleid, T. *Z. Anorg. Allg. Chem.* **2000**, *626*, 196–201.
(23) Sieke, C.; Schleid, T. *Z. Anorg. Allg. Chem.* **2001**, *627*, 761–767.
(24) Blasse, G.; Bril, A. *J. Inorg. Nucl. Chem.* **1967**, *29*, 2231–2241.
(25) Isaacs, T. J. *J. Electrochem. Soc.* **1973**, *120*, 654–656.
(26) Han, X. M.; Lin, J.; Xing, R. B.; Fu, J.; Wang, S. B.; Han, Y. C. *J. Phys. Condens. Matter* **2003**, *15*, 2115–2126.
(27) de Sá, G. F.; Malta, O. L.; de Mello Donegá, C.; Simas, A. M.; Longo, R. L.; Santa-Cruz, P. A., Jr *Coord. Chem. Rev.* **2000**, *196*, 165–195.
(28) van Pierterson, L.; Reid, M. F.; Burdick, G. W.; Meijerink, A. *Phys. Rev. B* **2002**, *65*, 45113–45128.

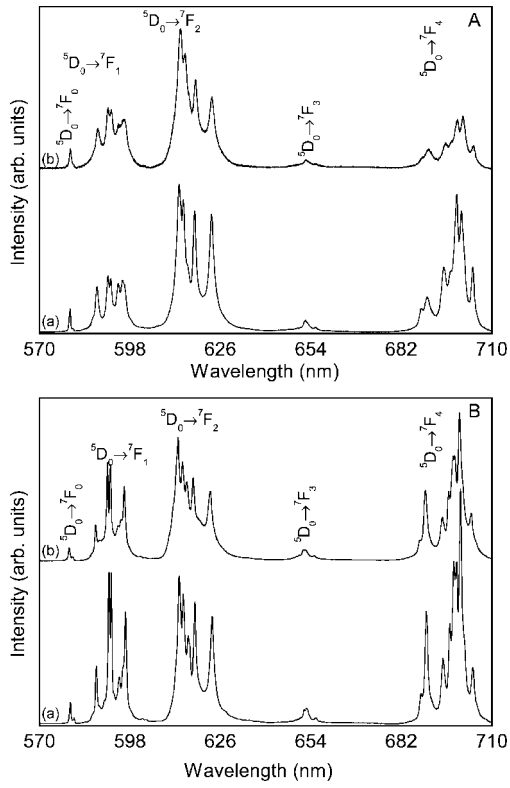

Figure 7. Emission spectra excited at 394 nm of the $(Eu_{0.125}Gd_{0.875})_2(SiO_4H)(OH)_2(H_2O)Cl$ (a) and $Eu_2(SiO_4H)(OH)_2(H_2O)Cl$ (b) recorded at (A) room temperature and (B) 10 K.

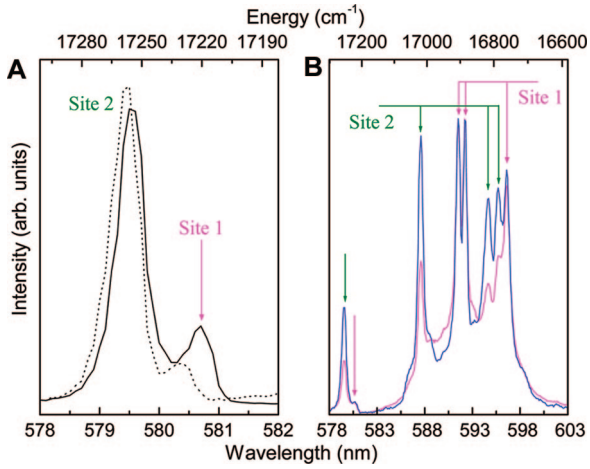

Figure 8. Magnification of the Eu^{3+} (A) $^5D_0 \rightarrow {}^7F_0$ region acquired at room temperature (black line) and 10 K (dotted line) and excited at 394 nm and (B) $^5D_0 \rightarrow {}^7F_{0,1}$ transitions collected at 10 K and excited at 273 nm, the $^6I_{J/2}$ level of Gd^{3+} (magenta line), and at 465 nm, the $^5D_2$ level of Eu^{3+} (blue line) for $(Eu_{0.125}Gd_{0.875})_2(SiO_4H)(OH)_2(H_2O)Cl$.

Figure 7 shows the emission spectra of two selected Eu^{3+}-doped silicates. The sharp lines are assigned to transitions between the first excited nondegenerate $^5D_0$ state and the $^7F_{0-4}$ levels of the fundamental Eu^{3+} septet. Except for the $^5D_0 \rightarrow {}^7F_1$ lines, which have a predominant magnetic-dipole character, the observed transitions are mainly of the electric-dipole nature. The presence of two lines (ca. 17 224 and 17 255 cm^{-1}; ca. 580.6 and 579.5 nm, respectively) for the nondegenerated $^5D_0 \rightarrow {}^7F_0$ transition (Figure 8A) and the local-field splitting of the $^7F_1$ level in six Stark components (Figure 8B) suggest the presence of two different Eu^{3+} environments, in accordance with the crystal structure. Although the number of emission lines and their energy, of $Eu_2(SiO_4H)(OH)_2(H_2O)Cl$ and Eu^{3+}/Gd^{3+} mixed materials, are similar, at room temperature the intensity of the $^5D_0 \rightarrow {}^7F_4$ transition is smaller for the former (Figure 7A). At 10 K, all emission spectra are analogous (Figure 7B).

Consider now the variation of the relative intensity of the $^7F_{1,2}$ Stark components and $^5D_0 \rightarrow {}^7F_0$ lines with the temperature (Figure 7A,B). The thermally activated nonradiative channel associated with the OH oscillators is more important for site 1 (four OH and one H_2O) than for site 2 (three OH) (Figure 3) and is responsible for such intensity changes. Therefore, site 1 exhibits (i) a $^5D_0 \rightarrow {}^7F_1$ magnetic transition stronger than the $^5D_0 \rightarrow {}^7F_2$ forced electric-dipole transition and (ii) a relatively weak $^5D_0 \rightarrow {}^7F_0$ transition (Figure 8A). For site 2, the $^5D_0 \rightarrow {}^7F_2$ transition dominates and the $^5D_0 \rightarrow {}^7F_0$ transition is relatively strong, typical of a distorted site with low symmetry. The fact that the coordination sphere of Eu(1) is approximately centrosymmetric is entirely compatible with the observed $^5D_0 \rightarrow {}^7F_4$ abnormally high intensity (Figure 7A,B).[29] The attribution of the PL features of each site may also be rationalized in terms of the relationship between the covalency of the local Eu^{3+} environments, the nephelauxetic effect (affecting the energy of the $^5D_0 \rightarrow {}^7F_0$ transition),[30] and the energy difference between the outer $^7F_1$ Stark components $-\Delta E(^7F_1)$.[31] Data indicate that the local environment of Eu(1) is more covalent than that of Eu(2), respectively $^5D_0 \rightarrow {}^7F_0$ transition energy, ca. 17 224 and 17 255 cm^{-1}, $\Delta E(^7F_1)$ ca. 144 and 231 cm^{-1}. Moreover, for the Eu^{3+}/Gd^{3+} samples, excitation at low temperature into the Gd^{3+} lines favors the emission of site 1, relative to the excitation within the $^5D_2$ Eu^{3+} level (Figure 8B). In fact, as far as the first sphere of Ln−Ln distances are concerned, the average Ln(2)···Ln is longer than the average Ln(1)···Ln one, respectively 3.89 and 3.75 Å.

The room-temperature $^5D_0$ lifetimes were determined under direct intra-$4f^6$ excitation ($^5L_6$, 393 nm) by monitoring the emission decay curves within the $^5D_0 \rightarrow {}^7F_1$ transition at 590.2 nm (site 1) and 586.8 nm (site 2). All decay curves are well reproduced by single-exponential functions (not shown), yielding for $(Eu_xGd_{1-x})_2(SiO_4H)(OH)_2(H_2O)Cl$, $x = 1.00$, 0.50, and 0.125, $^5D_0$ lifetime values of, respectively, 0.216 ± 0.001, 0.341 ± 0.002, and 0.356 ± 0.003 ms (site 1) and 0.206 ± 0.002, 0.333 ± 0.003, and 0.415 ± 0.003 ms (site 2). Except for the lower Eu content sample, the lifetimes of sites 1 and 2 are similar, despite the fact that the metal coordination spheres are different. Increasing the Eu concentration also increases the energy exchange between all Eu^{3+}, decreasing both lifetimes. On the other hand, the first coordination sphere of Eu(1) contains six OH oscillators (four OH and one H_2O), which essentially determine the site lifetime. Because Eu(2) is coordinated by fewer (three) OH groups,

(29) Ferreira, R. A. S.; Nobre, S. S.; Granadeiro, C. M.; Nogueira, H. I. S.; Carlos, L. D.; Malta, O. L. *J. Lumin.* **2006**, *121* (2), 561–567.
(30) Carlos, L. D.; Malta, O. L.; Albuquerque, R. Q. *Chem. Phys. Lett.* **2005**, *415*, 238–242.
(31) Carnall, W. T.; Crosswhite, H.; Crosswhite, H. M. *Energy Level Structure and Transition Probabilities of the Trivalent Lanthanides in LaF3*; Argonne National Laboratory: Argonne, IL, 1977.

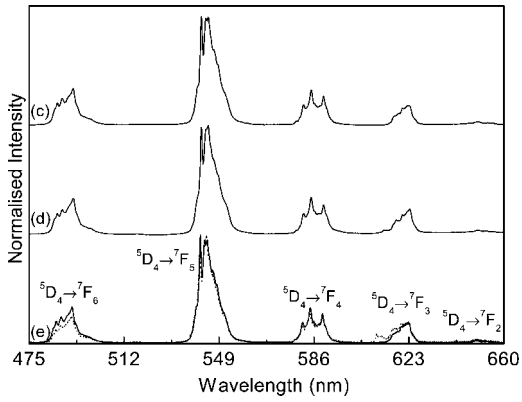

Figure 9. Room-temperature emission spectra of the $(Tb_{0.1}Gd_{0.9})_2(SiO_4H)(OH)_2(H_2O)Cl$ (c), $(Tb_{0.5}Gd_{0.5})_2(SiO_4H)(OH)_2(H_2O)Cl$ (d), and $Tb_2(SiO_4H)(OH)_2(H_2O)Cl$ (e) samples excited at 377 nm. The 10 K emission spectrum of the $Tb_2(SiO_4H)(OH)_2(H_2O)Cl$ sample is also shown (dotted line).

Table 4. Absolute Emission Quantum Yield Values of the Eu^{3+}- and Tb^{3+}-Based Silicates under Different Excitation Wavelengths (λ_{ex})

	λ_{ex} (nm)		
sample	394	380	274
$Eu_2(SiO_4H)(OH)_2(H_2O)Cl$	0.03		
$(Gd_{0.875}Eu_{0.125})_2(SiO_4H)(OH)_2(H_2O)Cl$	0.09		0.06
$Tb_2(SiO_4H)(OH)_2(H_2O)Cl$		0.01	
$(Tb_{0.9}Gd_{0.1})_2(SiO_4H)(OH)_2(H_2O)Cl$		0.02	0.03
$(Tb_{0.5}Gd_{0.5})_2(SiO_4H)(OH)_2(H_2O)Cl$		0.03	0.07
$(Tb_{0.1}Gd_{0.9})_2(SiO_4H)(OH)_2(H_2O)Cl$		0.04	0.12

the contribution of Eu−Eu quenching effects for the decreasing of lifetimes is likely to be more significant.

The $(Tb_xGd_{1-x})_2(SiO_4H)(OH)_2(H_2O)Cl$ ($x = 0.1$, 0.5, 0.9, and 1) samples are also emitters between 10 K and room temperature (Figure 9). The increase of the Tb^{3+}/Gd^{3+} ratio does not produce major changes in the emission features. The room-temperature $^5D_4$ lifetimes were determined under direct intra-$4f^8$ excitation ($^5D_3$, 377 nm) by monitoring of the $^5D_4 \rightarrow {}^7F_5$ transition. The curves are biexponential, yielding for $(Tb_xGd_{1-x})_2(SiO_4H)(OH)_2(H_2O)Cl$, $x = 1.00$, 0.50, and 0.10, lifetimes of respectively 0.273 ± 0.015, 0.401 ± 0.008, and 1.360 ± 0.013 ms (site 1) and 0.034 ± 0.001, 0.070 ± 0.005, and 0.093 ± 0.002 ms (site 2). The decrease in the two lifetime values as the Tb^{3+}/Gd^{3+} ratio increases points out the presence of Tb^{3+} concentration quenching effects.

The emission features of the silicates were quantified through the measurement of the emission quantum yield (ϕ) under direct intra-4f excitation, namely, the Eu^{3+} intra-$4f^6$ $^5L_6$ at 393 nm and the Tb^{3+} intra-$4f^8$ $^5D_3$ at 380 nm. As gathered in Table 4, the ϕ values are within the intervals 0.03–0.09 and 0.01–0.04 for the Eu^{3+}- and Tb^{3+}-based silicates, respectively. These values are substantially smaller than those of Ln-based silicate inorganic phosphors, such as oxyapatites (20–30%), but are similar to those reported for Eu^{3+} hexagonal[32] and Eu^{3+}-doped apatite-type[33] silicates.

For the Gd-diluted silicates, the absolute emission was also estimated under excitation via the Gd^{3+} excited states (274 nm, $^8S_{7/2}$). For Tb^{3+}-based silicates, an increase in the ϕ values relative to those measured under intra-$4f^8$ excitation is observed, suggesting that the Gd^{3+} excited levels are an effective channel in the population of the $^5D_4$. For the Eu^{3+} silicates, the opposite behavior is observed; the ϕ values are smaller under excitation at 274 nm (the Gd^{3+} $^8S_{7/2}$ level). This may be related to the fact that the $^8S_{7/2}$ level overlaps the LMCT band, which is consistent with the fact that LMCT states constitute an important channel for depopulation of the lanthanide excited states, leading to luminescence quenching.[34] For both silicate materials and independently of the excitation wavelength, it is observed that the emission quantum yield values increase with the amount of Gd^{3+} ions, suggesting that the Gd^{3+} excited levels are an effective channel in the population of the $^5D_0$ (Eu^{3+}) and $^5D_4$ (Tb^{3+}) levels, and it is also consistent with the above suggestion that concentration quenching effects are present in the silicates with higher relative concentrations of Eu^{3+} and Tb^{3+}, as was previously suggested for Eu^{3+}-doped apatite-type silicates.[33]

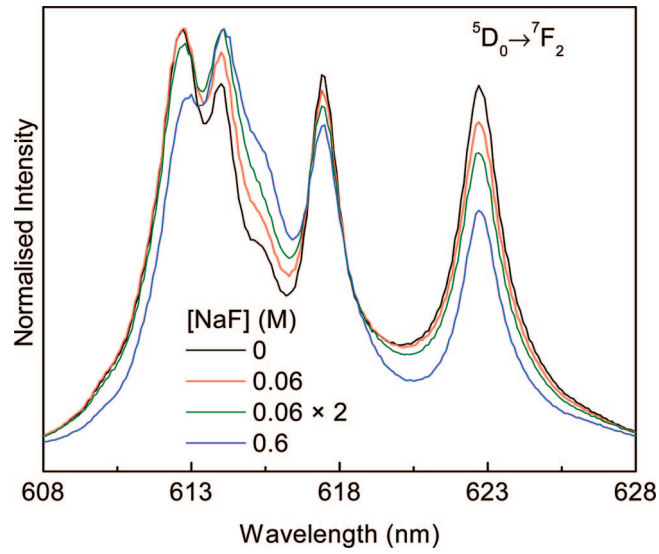

Figure 10. Emission spectra of $(Eu_{0.125}Gd_{0.875})_2(SiO_4H)(OH)_2(H_2O)Cl$ recorded at room temperature and excited at 394 nm before and after ion exchange with F^-. Ion exchange was performed by stirring a suspension of $(Eu_{0.125}Gd_{0.875})_2(SiO_4H)(OH)_2(H_2O)Cl$ (0.006 mol/dm^3 of solution) with NaF at 80 °C for two cycles of 20 h.

Because the relatively long bond distance of 2.81 Å suggests a predominantly ionic interaction between Eu(2) and Cl(1) (it is approximately the sum of the ionic radii of the ions), we have attempted to ion exchange Cl^- by F^-. Preliminary EDS, XPS, and PL experiments suggest that, indeed, some Cl^- is exchanged. The emission spectra of the mixed Eu^{3+}/Gd^{3+} sample exchanged with increasing F^- (Figure 10) exhibit clear modifications relative to the spectrum of the parent material, particularly in the relative intensity of the Stark components of the $^5D_0 \rightarrow {}^7F_2$ transition. These observations raise two interesting questions. First, the layered materials reported here are, perhaps, reminiscent of layered double hydroxides, con-

(32) Blasse, G.; Bril, A. *J. Inorg. Nucl. Chem.* **1967**, *29*, 2231.
(33) Ferdov, S.; Ferreira, R. A. S.; Lin, Z. *Chem. Mater.* **2006**, *18*, 5958.
(34) Struck, C. W.; Fonger, W. H. *Understanding Luminescence Spectra and Efficiency Using Wp and Related Functions*; Springer: Berlin, 1991;and references cited therein.

sisting of cationic layers with exchangeable anions in the interlayer space. Second, the materials may be used in a PL sensor for (at least) Cl^- and F^-.

Acknowledgment. This work was supported by Fundação para a Ciência e a Tecnologia, PTDC, FEDER, and NoE FAME. We thank Dr. I. Margiolaki for assistance with the XRD experiments at ID31 ESRF and Dr. N. Pinna for the TEM images.

Supporting Information Available: Figures S1 and S2 and Tables S1 and S2. This material is available free of charge via the Internet at http://pubs.acs.org.

CM702524N